Applied Catalysis B: Environmental 249 (2019) 126–137

Contents lists available at ScienceDirect

Applied Catalysis B: Environmental

journal homepage: www.elsevier.com/locate/apcatb

Enhanced photocatalytic NO*x* oxidation and storage under visible-light irradiation by anchoring Fe_3O_4 nanoparticles on mesoporous graphitic carbon nitride (*mpg*-C_3N_4)

Muhammad Irfan[a,e], Melike Sevim[b], Yusuf Koçak[a], Merve Balci[a], Önder Metin[c,*], Emrah Ozensoy[a,d,*]

[a] Chemistry Department, Bilkent University, 06800, Bilkent, Ankara, Turkey
[b] Chemistry Department, Atatürk University, 25240, Yakutiye, Erzurum, Turkey
[c] Chemistry Department, Koç University, 34450, Sariyer, Istanbul, Turkey
[d] UNAM-National Nanotechnology Center, Bilkent University, 06800, Ankara, Turkey
[e] Nanoscience and Catalysis Department, National Centre for Physics, 44000, Islamabad, Pakistan

ARTICLE INFO

Keywords:
Graphitic carbon nitride
Iron oxide
Photocatalytic oxidation
NOx abatement
DeNOx

ABSTRACT

Several mesoporous graphitic carbon nitride (*mpg*-C_3N_4) photocatalysts were synthesized by using a hard-templating method comprising thermal polycondensation of guanidine hydrochloride over silica spheres at three different temperatures (450, 500 and 550 °C). After structural characterization of these *mpg*-C_3N_4 photocatalysts, they were tested in NO(g) photo-oxidation under visible (VIS) light. The effects of polycondensation temperature on the structure and photocatalytic performance of *mpg*-C_3N_4 in NO photo-oxidation were studied. The results revealed that polycondensation temperature has a dramatic effect on the photocatalytic activity of *mpg*-C_3N_4 in NO photo-oxidation, where *mpg*-C_3N_4 synthesized at 500 °C (*mpg*-CN500) showed the best performance in NO_x abatement as well as a high selectivity towards solid state NO_x storage under VIS light illumination. Photocatalytic performance of the *mpg*-CN500 was further enhanced by the anchoring of 8.0 ± 0.5 wt.% Fe_3O_4 nanoparticles (NPs) on it. Fe_3O_4/*mpg*-CN500 photocatalyst showed both high activity and high selectivity along with extended reusability without a need for a regeneration step. Enhanced photocatalytic NO_x oxidation and storage efficiency of Fe_3O_4/*mpg*-CN500 photocatalyst was attributed to their mesoporous structure, high surface area and slow electron-hole recombination kinetics, efficient electron-hole separation and facile electron transfer from *mpg*-CN500 to Fe_3O_4 domains enhancing photocatalytic O_2 reduction, while simultaneously suppressing nitrate photo-reduction and decomposition to NO_2(g).

1. Introduction

Atmospheric pollution is considered to be one of the major threats for modern society. Anthropogenic air pollutants such as nitrogen oxides (NO_x) induce ozone production in troposphere and cause acid rains. Particularly, nitric oxide (NO) and nitrogen dioxide (NO_2) severely affect human respiratory and immune systems [1–3]. Although NO_x emissions have been strictly regulated by the environmental protection agencies, the recommended value of ≤ 0.2 ppm is often exceeded in urban settings [4]. Therefore, finding improved approaches for NO_x removal from the atmosphere is essential. Although NO_x abatement can be performed efficiently using thermal catalytic technologies (*i.e.* selective catalytic reduction/SCR and NO_x storage and reduction/NSR) at elevated temperatures [5–8], an important challenge is the abatement of gaseous NO_x species under ambient conditions (*i.e.* at room temperature and atmospheric pressure).

In this regard, semiconductor photocatalysis presents an appealing alternative, since the major requirements for these technologies are only sunlight, water and oxygen which are naturally present in the atmosphere in abundance [9]. This approach has been already implemented in advanced construction materials to combat urban NO_x pollution, using mainly titania (TiO_2) based photocatalysts [10–12]. Despite its favorable properties like chemical inertness, long-term stability and low cost, TiO_2 has a typical band gap of 3.0–3.2 eV. This large band gap enables the harvesting of mostly UV light, which constitutes only 4–5% of the incoming solar energy [13,14]. More importantly, in photocatalytic NO_x abatement applications, TiO_2 has a low selectivity towards NO_x storage in solid state and tends to oxidize NO(g) into a

* Corresponding author.
E-mail addresses: ometin@ku.edu.tr (Ö. Metin), ozensoy@fen.bilkent.edu.tr (E. Ozensoy).

https://doi.org/10.1016/j.apcatb.2019.02.067
Received 29 November 2018; Received in revised form 8 February 2019; Accepted 23 February 2019
Available online 25 February 2019
0926-3373/

more toxic product, NO_2(g) [15]. Therefore, it is necessary to develop alternative photocatalysts harvesting a broad wavelength window with high efficiency and stability. Moreover, the proposed $DeNO_x$ materials should be abundant, accessible, easy to synthesize, stable and non-toxic in order to justify their implementation on a large scale.

Among such potential photocatalytic systems, two-dimensional (2D) graphitic carbon nitride (*g*-C_3N_4) is one of the strong contenders owing to its metal-free nature, thermal stability, non-toxicity, low-cost and relatively narrow band gap (2.7 eV, 454 nm) falling in the visible range of the solar spectrum [16]. These unique properties make *g*-C_3N_4 as an attractive candidate for various applications in the field of solar energy conversion and environmental remediation [17]. The uniquely versatile 2D-layered polymeric structure of *g*-C_3N_4 which mainly consists of carbon and nitrogen atoms along with a minor amount of H atoms (*e.g.* at termination and defects sites) can be synthesized using different approaches including polycondensation, pyrolysis, solvothermal and physical/chemical vapor deposition [18,19]. However, *g*-C_3N_4 has a very low surface area (10-50 m^2/g) which limits its practical photocatalytic applications. To overcome this drawback, mesoporous graphitic carbon nitride (*mpg*-C_3N_4) can be prepared by template-assisted methods that are particularly beneficial as they enable fine-tuning of the surface, electronic, and morphological properties of *g*-C_3N_4 and also allow the design of highly porous structures with a large surface area (150-400 m^2/g) [20]. Mesoporous photocatalytic structures with a large surface area can increase the number of exposed active sites of the photocatalyst, which in turn, can improve the photocatalytic activity through enhanced solar light absorbance capacity.

It is well known that photo-oxidation and storage of NO(g) in the form of solid state nitrate species is a complex process and involves several intermediates such as nitrogen dioxide (NO_2(g)) [15]. It is important to note that NO_2(g) is far more toxic than NO(g) as it can contribute towards formation of secondary pollutants like acid rain. Thus, extensive release of NO_2(g) at the end of the photocatalytic process can nullify the overall photocatalytic NO_x abatement effect [21]. Therefore, it is of paramount importance to design photocatalysts which restrict the formation and/or emission of toxic side-products such as NO_2(g). Designing such a photocatalyst is a challenge as increased selectivity can also sacrifice photocatalytic activity.

Photocatalytic architectures containing *mpg*-C_3N_4 can be enhanced using a variety of synthetic strategies. Among these strategies, addition of non-precious transition metals is one of the most effective and convenient approaches to introduce desired properties into the *mpg*-C_3N_4 photocatalyst system. Magnetite (Fe_3O_4) is a common form of iron oxide containing both Fe^{2+} and Fe^{3+} cationic species in a spinel structure. It has been demonstrated that Fe_3O_4 could be utilized as a promising catalytic promoter due to its unique electronic and magnetic properties [22–24]. In this context, in the current study, we integrate Fe_3O_4 nanoparticles (NPs) and 2D *mpg*-C_3N_4 nanosheets in a single nanocomposite system as an efficient and inexpensive photocatalyst for airborne NO_x abatement.

In the present study, several *mpg*-C_3N_4 photocatalysts were synthesized by using a hard-templating method comprising thermal polycondensation of guanidine hydrochloride (GndCl) over silica spheres at three different temperatures (450-550 °C). The structure of as-synthesized photocatalysts were characterized by using a multitude of analytical techniques. Thereafter, photocatalytic performances of these photocatalysts were tested in NO photo-oxidation under environmentally relevant reaction conditions. Moreover, the photocatalytic performance of the *mpg*-CN500 in NO oxidation was further enhanced by the assembly of 8.0 ± 0.5 wt.% Fe_3O_4 NPs on it.

2. Materials and methods

Iron (III) acetylacetonate [Fe(acac)$_3$, 99.9%], oleylamine (> 70%), benzyl ether (98%), Ludox® HS-40 (40 wt.% colloidal SiO_2 suspension in water) and Titanium (IV) oxide (P25, ≥99.5%) were purchased from Sigma-Aldrich. Guanidine hydrochloride (GndCl, 98%) and ammonium hydrogen difluoride (NH_4HF_2, 98.5%) were purchased from Alfa-Aesar and Fluka, respectively. All chemicals used in this work were used as received without further purification.

2.1. Synthesis of the mpg-C_3N_4

The *mpg*-C_3N_4 photocatalysts were prepared by the thermal polycondensation of GndCl in the presence of Ludox® HS-40 colloidal silica as a hard template. In a typical synthesis campaign [25], 4.0 g of GndCl was dissolved in 4 mL distilled water in a glass vial and added dropwise into 10 g of Ludox® HS40 colloidal silica under vigorous stirring. The resultant mixture was kept at 50 °C for overnight. Obtained white solid was crushed in a ceramic mortar and was placed into a quartz crucible with a cover for annealing. The crucible was heated in a horizontal quartz-tube oven at 450, 500 and 550 °C for 2 h with a ramp rate of 4–5 °C min-1 under argon flow. The resultant products were denoted as *mpg*-CN450, *mpg*-CN500 and *mpg*-CN550, respectively. Next, the yellow solid powders attained *via* this approach were reacted with 4 M, 200 mL of NH_4HF_2 (aq) solution for two days to remove the silica template. Finally, obtained powders were repeatedly washed with water and ethanol in order to remove the residual reactants and dried overnight at *ca.* 50 °C in a vacuum oven.

2.2. Synthesis of Fe_3O_4 nanoparticles

Monodisperse Fe_3O_4 nanoparticles were synthesized by using a well-established protocol published elsewhere [26]. In a typical synthesis, 3 mmol of Fe(acac)$_3$ was dissolved in 15 mL of benzyl ether and 15 mL of oleylamine. The resultant solution was heated to 120 °C and kept at this temperature for 1 h under nitrogen atmosphere. Next, the resultant mixture was quickly heated to 300 °C, and kept at this temperature for 1 h. Then, the solution was cooled to room temperature. To purify and separate the Fe_3O_4 nanoparticles (NPs), ethanol was added to the reaction mixture and the mixture was centrifuged for 12 min at 8500 rpm. Separated Fe_3O_4 NPs were dispersed in hexane for the further use.

2.3. Incorporation of the mpg-C_3N_4 with Fe_3O_4 NPs

In a typical procedure, 50 mg of monodisperse Fe_3O_4 NPs were added to 10 mL of hexane and then mixed with 150 mg of *mpg*-CN500 sample which was initially dispersed in 30 mL of ethanol. The resultant ethanol/hexane mixture was sonicated for 2 h to ensure adsorption of the Fe_3O_4 NPs onto *mpg*-CN500. Next, the resultant mixture was centrifuged at 7500 rpm for 10 min and the separated nanocomposite (containing both *mpg*-CN500 and Fe_3O_4) was washed with ethanol for several times and dried under vacuum. These samples will be referred as Fe_3O_4/*mpg*-CN500 in the rest of the text. Fe_3O_4 content of the synthesized Fe_3O_4/*mpg*-CN500 materials was determined by ICP-MS analysis as 8.0 ± 0.5 wt.%. This apparently small Fe_3O_4 loading is due to the removal of oleylamine (OAm), a long chain (C18) organic molecule which was used as surfactant for the synthesis of Fe_3O_4 NPs. In other words, 50 mg Fe_3O_4 sample actually included a much lesser amount of pure Fe_3O_4.

2.4. Structural characterization

Crystal structures of the synthesized materials were analyzed using a PANalytical Empyrean XRD diffractometer equipped with Cu-Kα radiation (40 kV, 45 mA, λ = 1.54051 Å). Attenuated Total Reflectance (ATR) Fourier transform-infrared (FTIR) spectra were collected using a Bruker Alpha Eco-ATR spectrometer in the frequency range of 400–4000 cm^{-1}. The optical absorption properties of the samples were investigated *via* Diffuse Reflectance UV-VIS (DR-UV-VIS) Spectroscopy using a Cary 5000 UV-VIS-NIR Spectrometer equipped with a Varian

Cary 2500 Internal Diffuse Reflectance (DR) Accessory. The Brunauer-Emmett-Teller (BET) specific surface area (SSA) measurements of the synthesized catalysts were carried out using nitrogen adsorption–desorption isotherms obtained with a Micromeritics 3Flex surface area and pore size analyzer. Prior to SSA analysis, all samples were outgassed in vacuum for 2 h at 150 °C. X-ray photoelectron spectroscopy (XPS) experiments were performed with a SPECS PHOIBOS hemispherical energy analyzer. A monochromatic Al-Kα X-ray excitation source (15 kV, 400 W) was employed during the XPS data acquisition. Transmission electron microscopy (TEM), Scanning transmission electron microscopy (STEM), High Angle Annular Dark Field (HAADF) imaging and Energy Dispersive X-Ray (EDX) analysis experiments were carried out at 300 kV using an FEI Technai G2 F30 Transmission Electron Microscope equipped with BF-/DF-STEM-EDX modules. The photoluminescence (PL) spectra were performed at room temperature using a Jobin-Yvon Horiba Fluorolog-3 equipped with a Hamamatsu R928 P detector and a 450 W ozone-free Osram XBO xenon arc lamp. The excitation wavelength was 390 nm which is well above the sample band gap. The fluorescence was monitored at a right angle relative to the excitation. Sonication experiments was performed in a VWR USC 900 T Ultrasonic Cleaner Bath (9.2 L, 45 kHz) at room temperature. Temperature of the sonication bath was kept below 30 °C *via* ice addition into the bath. Without any ice addition, the final temperature of the sonication bath reached up to 40 °C after 2 h.

2.5. Photocatalytic activity measurements

The photocatalytic DeNOx experiments were performed at room temperature in flow mode by considering the experimental requirements that were reported in the ISO 22197-1 standard [27]. Inlet gas mixture that was introduced to the reactor (Fig. S1) contained 0.750 standard liters per minute (SLM) N_2 (g) (purity: 99.99%, Linde GmbH), 0.250 SLM O_2 (purity: 99%, Linde GmbH) and 0.010 SLM NO (100 ppm NO (g) diluted in balance N_2 (g), Linde GmbH). In order to obtain the gas flow values given above, mass flow controllers (MFCs, MKS1479 A for N_2 (g) and O_2 (g) and Teledyne HFC-202 for NO (g) diluted in N_2 (g)) were utilized so that the typical total gas flow over the photocatalyst was stabilized at 1.010 SLM ± 0.05 SLM, where the NO (g) content of the inlet gas mixture was fixed at 1 ppm. The pressure inside the reactor was kept at *ca.* 1 bar and measured *via* a MKS Baratron 622B capacitance manometer. Humidity of the inlet gas mixture was also carefully controlled by dosing varying amounts of water vapor into the inlet gas mixture (*i.e.* before the reactor entrance) with the help of a Perm Select (PDMSXA-2500) semi permeable membrane module attached to an external variable-temperature water chiller/recycler for controlling equilibrium vapor pressure of water. Typical relative humidity (RH) of the reactor was kept within 50 ± 3% at 23 ± 2 °C, measured at the sample position using a Hanna HI 9565 humidity analyzer. Changes in the NO, NO_2, and total NO_x gas concentrations at the outlet of the reactor were monitored using a chemiluminescent NO_x analyzer, Horiba Apna-370 with a 0.1 ppb sensitivity and 1 Hz (*i.e.* 1 measurement per second) detection speed.

For the experiments performed with VIS illumination, a 35 W metal halide lamp (HCI-TC 35 W/942 NDL PB 400–700 nm range, Osram) was utilized. Since the currently used VIS light source also emitted a limited but detectable flux of UV light, a commercial VIS-transparent UV-blocker/filtering film (LLumar window film UV CL SR PS (clear)) was placed on top of the reactor during the VIS-light experiments. This was crucial for ruling out any contribution from UV photons during the VIS-light illumination. Numerically, without using UVA filter, the UVA flux measured by the UVA probe (LP471 UVA, DeltaOhm) within 315–400 nm wavelength range was 2.092 W/m^2, while this value dropped by %99.93 to 0.015 W/m^2 in the presence of the UVA filter (with which the experiments were carried out). The incoming light flux was measured carefully at the sample position before and after each photocatalytic activity test with a photo-radiometer (HD2302.0, Delta Ohm/Italy) using a PAR VIS probe (400–700 nm). Typical VIS-light photon flux used in the current experiments was within 450–500 µmol/(m^{2}sec). Reactor temperature remained within 23–42 °C during a typical 60 min photocatalytic activity test with a VIS light source. In each performance analysis test, 200 mg of photocatalyst was packed in a 2 mm × 40 mm × 40 mm poly methyl methacrylate (PMMA) sample holder and placed into the flow reactor. In order to quantify the photocatalytic activity and selectivity, at the end of a typical 1 h photocatalytic activity test, obtained raw data was processed in order to obtain various figures of merit (such as percent photonic efficiency towards NO_x storage, percent photonic efficiency for NO_2 generation/release, percent NO conversion, percent selectivity towards NO_x storage, and DeNO_x index). Details of these figures of merit are explained in detail in the Supporting Information (SI) section.

3. Results and discussion

3.1. Electron microscopy analysis via TEM and STEM

Surface morphology of as-synthesized Fe_3O_4/mpg-CN500 sample was investigated *via* high- resolution TEM, STEM and High Angle Annular Dark Field (HAADF) imaging techniques as shown in Fig. 1. Since Fe_3O_4/*mpg*-CN500 sample revealed the highest photocatalytic performance (*vide infra*), this particular catalyst was chosen for the electron microscopy analysis. Images in Fig. 1a and b provide multiple views of the 2D (sheet-like) structure of the *mpg*-CN500 support material containing thin layers of *mpg*-C_3N_4 in Fe_3O_4/*mpg*-CN500 sample. Fig. 1c presents HAADF-STEM images revealing a general view of the dispersion and particle size variation of the Fe_3O_4 nanoparticles on the CN500 support. It is seen in Fig. 1c that average particle size of the Fe_3O_4 nanoparticles on the *mpg*-CN500 support material ranges within *ca.* 8–11 nm. Fig. 1d shows a HR-TEM image of a Fe_3O_4 nanoparticle with a diameter of *ca.* 8 nm located on the edge of the *mpg*-CN500 (*i.e.* *mpg*-C_3N_4) support material. Lattice fringes measured on this Fe_3O_4 nanoparticle yields an average spacing of 0.254 nm, which is in accordance with the (311) plane of magnetite (JCPDS card no. 19-0629). It should be noted that *g*-C_3N_4 has a distinct fringe spacing of 0.325 nm that corresponds to the inter-layer structural packing of (002) crystal plane (JCPDS 87–1526) [22,28].

3.2. Crystal structure analysis via XRD

Fig. 2 presents the XRD patterns of the synthesized *mpg*-CN450, *mpg*-CN500 and *mpg*-CN550 samples as well as the Fe_3O_4/*mpg*-CN500 catalyst along with the pure Fe_3O_4 reference material (JCPDS Card No: 19-0629). For pure *mpg*-CN450, *mpg*-CN500 and *mpg*-CN550 samples, two main diffraction peaks are observed at 27.5° and 13.2° which confirm the formation of graphitic carbon nitride (JCPDS Card No: 87-1526). Strong diffraction peak at 27.5° is a characteristic interplanar stacking feature of the conjugated aromatic system, indexed for *mpg*-C_3N_4 as the (002) peak. The small diffraction peak at around 13.2° corresponds to intralayer/in-plane diffraction of the continuous *tri-s*-triazine units and indexed as (100) [29]. With increasing calcination temperature within 450–550 °C, diffraction signal located at 2θ = 27.5° became sharper and the intensity of the diffraction peak at 2θ = 13.2° increased monotonically. Furthermore, weak features located at 2θ = 11.1° and 17.6° (due to impurities and minority phases) disappeared. These observations are in line with the ordering of the crystal structure of the *mpg*-C_3N_4 support material. Anchoring of the Fe_3O_4 NPs on *mpg*-C_3N_4 resulted in the appearance of a new set of characteristic diffraction signals that are in very good agreement with that of pristine Fe_3O_4 (JCPDS Card No: 19-0629) [22], which is also shown in Fig. 2. Addition of Fe_3O_4 NPs also led to broadening of the main *mpg*-C_3N_4 diffraction feature at 2θ = 27.5° indicating decreased crystallinity and increased disorder in the carbon nitride domains due to the presence of Fe_3O_4 NPs and host-guest interactions [30]. This observation may also imply a

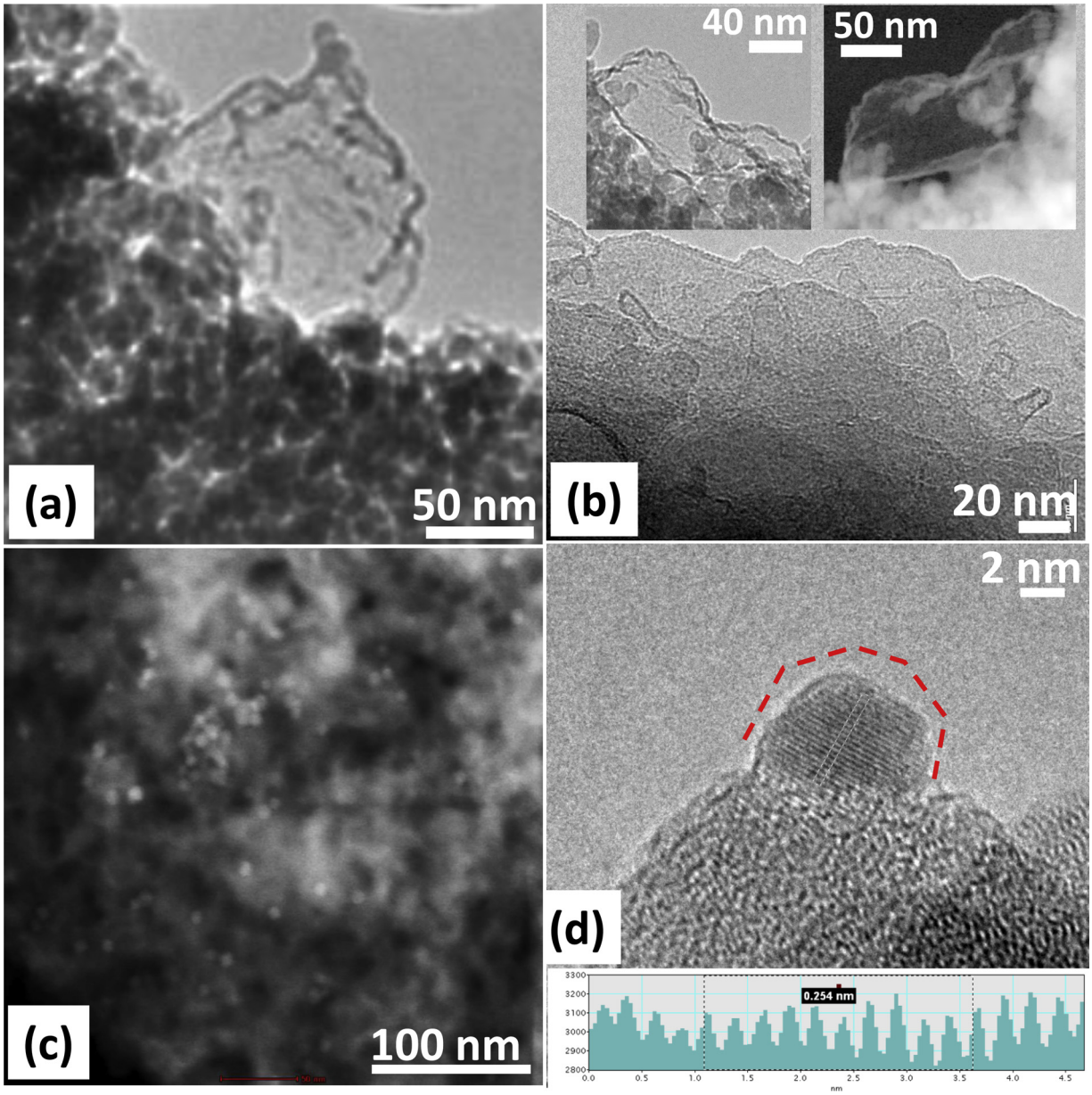

Fig. 1. (a–b) Multiple views of the 2D (sheet-like) structure of the *mpg*-C_3N_4 support material in Fe_3O_4/*mpg*-CN500. (c) HAADF-STEM image of Fe_3O_4/*mpg*-CN500 sample. (d) High-resolution TEM image of a Fe_3O_4 nanoparticle on the Fe_3O_4/*mpg*-CN500 photocatalyst (inset shows the distances between lattice fringes measured along the dashed white lines).

limited extend of incorporation of Fe species into the *mpg*-C_3N_4 matrix/layers.

3.3. Investigation of the surface composition via XPS

XPS measurements were performed in order to investigate the surface chemistry and functional groups present on the synthesized *mpg*-C_3N_4-based photocatalysts. Fig. 3a-d show the C*1s*, N*1s*, Fe*2p* and O*1s* regions of the XP spectra corresponding to the Fe_3O_4/*mpg*-CN500 sample, respectively. In one of our former reports [17], we have provided a detailed discussion about the interpretation of the XP spectra of *mpg*-C_3N_4 materials that have been synthesized in a similar (though not identical) fashion in the absence of Fe_3O_4. Thus, in the light of the information provided in this aforementioned report [17], we can discuss the prominent XPS features of the currently synthesized Fe_3O_4/*mpg*-CN500 photocatalyst.

Fig. 3a presents the C*1s* region of the XP spectra of Fe_3O_4/*mpg*-CN500 with a complex and a convoluted structure. It exhibits an intense high binding energy (B.E.) peak at 288.4 eV, which can be assigned to sp^2-hybridized carbon species. The feature at 286.9 eV can be attributed to a variety of carbon species bound to N-containing species such as, sp-bonded carbon atoms in C≡N groups [31], sp^2-hybridized s-triazine aromatic ring carbon, $(–N–)_2–C = N$ or sp^2-hybridized s-triazine aromatic ring carbon coordinated to the terminal amino group, $N–C(–NH_2) = N$ or carbon species bound to O-containing species. Note that readily detectable amounts of oxygen species are commonly observed in *mpg*-C_3N_4 structures, which can be located at the termination sites or defects/impurities in the s-triazine aromatic ring system of *mpg*-C_3N_4 [17]. C*1s* feature at 284.6 eV in Fig. 3a can be attributed to the C species that are mostly bound to other carbon atoms and also to adventitious carbon. Since in an ideal *mpg*-C_3N_4 structure containing interconnected s-triazine rings, there should not be any C—C/C = C linkages, presence of this feature implies the existence of carbonaceous impurities (*e.g.* graphite, graphene, graphene oxide *etc.*) in the *mpg*-

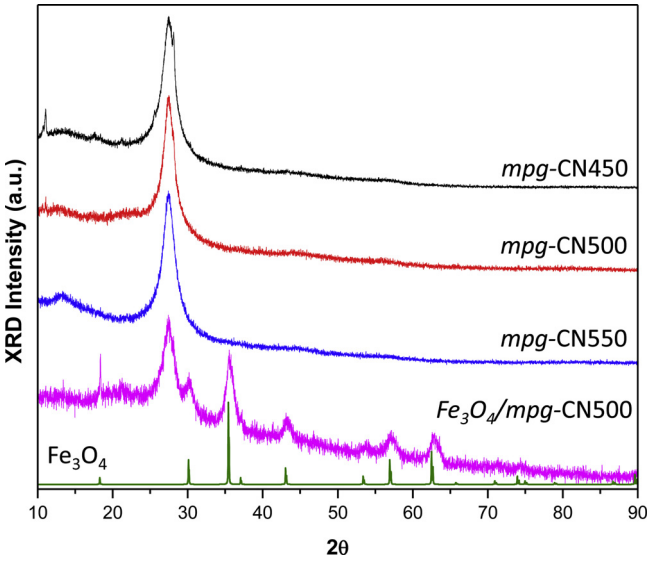

Fig. 2. XRD profiles of *mpg*-CN450, *mpg*-CN500, *mpg*-CN550 and Fe_3O_4/*mpg*-CN500 photocatalysts and pure Fe_3O_4 reference material.

C_3N_4 system. This was also observed in our former report on similar *mpg*-C_3N_4 materials [17,32]. Finally, XPS spectrum in Fig. 3a also contains a broad low B.E feature (281.6 eV), which can be tentatively assigned to C species connected to the Fe species of the Fe_3O_4 NPs and C species connected to the residual Si species originating from the colloidal silica template used in the synthesis [33,34].

N*1s* region of the XP spectra of Fe_3O_4/*mpg*-CN500 can be seen in Fig. 3b. The broad and convoluted N*1s* feature located at 401.9 eV can be ascribed to N connected to O species at terminations or defects [17,35] and/or C–NH_2 (amino) functionalities with a possible contribution from differential charging effects [36]. The N1s signal present at 399.0 eV can be assigned to C–N-C species in s-triazine rings [17]. The most prominent N1s feature observed at 397.2 eV is associated with N atoms connected to C atoms in the s-triazine rings and/or pyridinic N-species [37]. Remaining minor peak at 395.1 eV in Fig. 3b with a low B.E. is tentatively assigned to N bound to Fe species (*e.g.* Fe-NH_2, Fe-N *etc.*) [38]. It should be noted that XPS analysis of semiconductors such as graphitic carbon nitride requires special attention as the XP spectra is extremely sensitive to the charge compensation (*i.e.* electron flood gun parameters) that is used during the XPS analysis. Along these lines, referencing of the B.E. positions are also difficult to accomplish since: a) due to the large C-content of the sample, it is not perfectly clear which C1s peak corresponds to the adventitious C; b) since the sample is not electrically conducting and also not homogeneous in terms of its surface composition/surface electronic structure, differential charging phenomena can severely shift, broaden, intensify or attenuate C1s signals in a drastic manner. Example XPS measurements with different charge-compensation parameters are presented in the Supporting Information section (Fig. S4). Nevertheless, general features of the currently presented C1s and N1s spectra are in line with our former studies [17].

Fe*2p* B.E. region of the XP spectra of Fe_3O_4/*mpg*-CN500 are presented in Fig. 3c. It is known that Fe_3O_4 (magnetite) typically reveals Fe$2p_{1/2}$ and Fe$2p_{3/2}$ XPS features at 724.1 ± 1 eV and 710.6 ± 1 eV, while these features characteristically appear at 724.6 ± 1 eV and 711.0 ± 1 eV for Fe_2O_3 (hematite), respectively. Furthermore, another

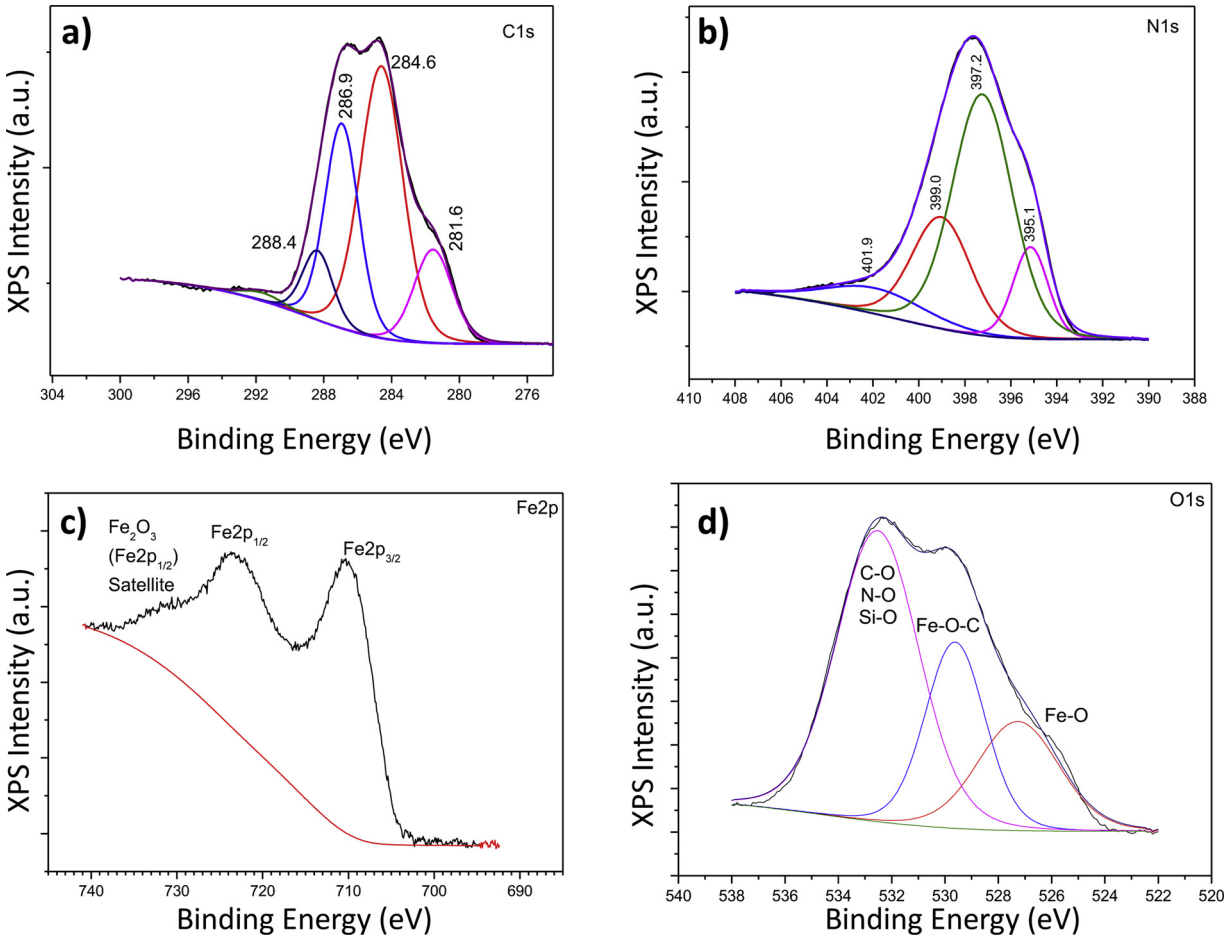

Fig. 3. XPS data for (a) C*1s*, (b) N*1s*, (c) Fe*2p*, and (d) O*1s* regions of Fe_3O_4/*mpg*-CN500 photocatalyst.

characteristic identifier for Fe_2O_3 is the satellite pair observed at 729.5 and 718.8 eV. On the other hand, Fe_3O_4 does not reveal such satellites [39,40]. Along these lines, XPS data in Fig. 3c suggest that both Fe_3O_4 and Fe_2O_3 species coexist in the Fe_3O_4/*mpg*-CN500 system. Lack of any Fe_2O_3 diffraction features in the XRD data presented in Fig. 2 indicates that Fe_2O_3 species may exist as disordered/amorphous minority domains or they may exist as an amorphous surface oxide covering the Fe_3O_4 nanoparticles forming a core-shell structure. The latter structure can be formed upon oxidation of Fe_3O_4 nanoparticles during calcination in air to form a surface Fe_2O_3 overlayer.

O*1s* XP spectrum for Fe_3O_4/*mpg*-CN500 given in Fig. 3d reveals a complex and a convoluted structure possessing contributions from a large variety of oxygen species. Hence, we will not attempt a detailed deconvolution of this data but rather mention some of the possible prominent species that might be associated with the spectrum. O*1s* data in Fig. 3d shows features at 532.5 eV, 529.6 eV and 527.2 eV. The feature observed at 532.5 eV is most likely associated with oxygen species bound to C, N and Si in different configurations [35,41,42]. The O*1s* feature located at *ca.* 529.6 eV can be attributed to Fe-O-C species while the shoulder at 527.2 eV is assigned to Fe-O species and/or differential charging features [41,43].

3.4. Bulk chemical composition via ATR-FTIR spectroscopy

ATR-FTIR spectroscopy was used to investigate the vibrational characteristics and surface functional groups of the synthesized *mpg*-C_3N_4 photocatalysts (Fig. 4). The broad bands in the 3000–3500 cm^{-1} region can be attributed to the N—H stretchings corresponding to the hydrogenation of terminal nitrogen atoms in *mpg*-C_3N_4 structures or N—H functionalities located at the surface defect sites [29]. The relatively weaker band at 2181 cm^{-1} can be assigned to the –C ≡N triple bond stretchings of cyano groups in the *mpg*-C_3N_4 structure. These cyano/cyanide as well as other uncondensed defects like NH_2/NH, −OH, −COOH are unavoidable as *mpg*-C_3N_4 structure evolves through the formation of several intermediates, such as cyanuric acid and melon [17]. It is interesting to note that the peak at 2181 cm^{-1} is more prominently observed only at higher processing temperature *i.e.* 550 ^{0}C or by the introduction of Fe_3O_4 NPs. IR adsorption band at 1617 cm^{-1} can be ascribed to the C═N stretching vibration modes, while the 1568, 1408, 1317 and 1238 cm^{-1} vibrational features are attributed to the typical stretching modes of the C–N aromatic heterocycles [44]. The absorption band at 806 cm^{-1} is assigned to the out of plane bending

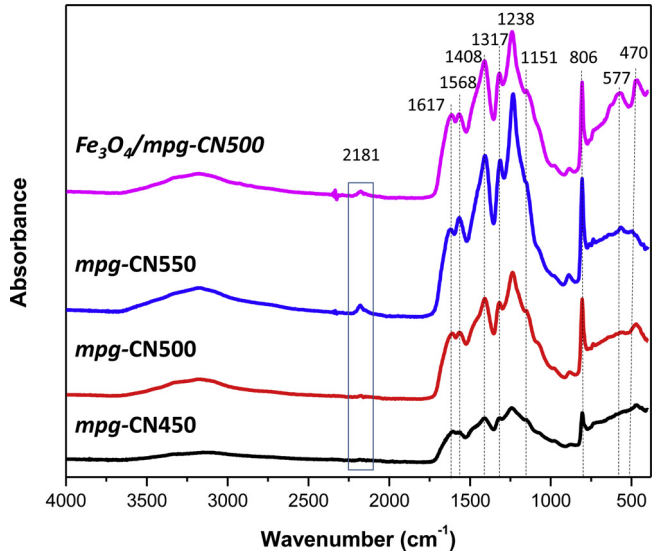

Fig. 4. ATR-FTIR spectra of *mpg*-CN450, *mpg*-CN500, *mpg*-CN550 and Fe_3O_4/*mpg*-CN500 photocatalysts.

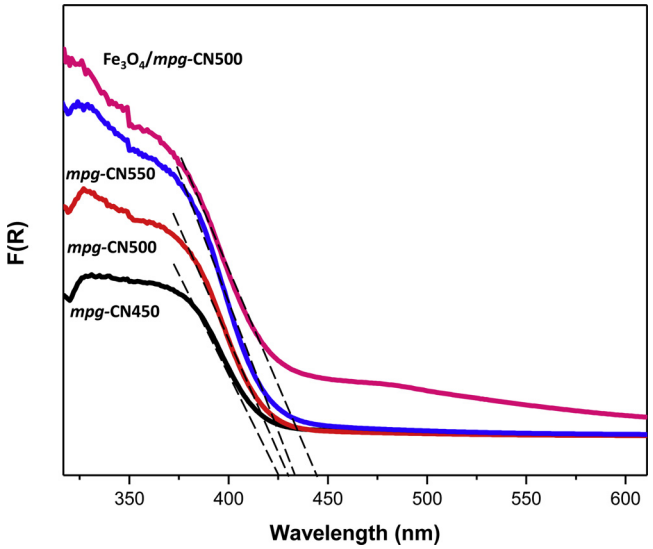

Fig. 5. a) DR-UV-VIS spectra of *mpg*-CN450, *mpg*-CN500, *mpg*-CN550 and Fe_3O_4/*mpg*-CN500 photocatalysts; b) Schematic representation of one of the possible Fe inclusion sites inside *mpg*-CN500 layers.

mode of triazine units [29]. The bands of the *mpg*-C_3N_4 photocatalysts become sharper with increasing calcination temperature because of the more ordered packing of the polymeric triazine units. The FTIR spectrum of Fe_3O_4/*mpg*-CN500 in Fig. 4 also shows two additional low frequency stretching bands that can be attributed to Fe_3O_4. The band at 577 cm^{-1} is associated with the Fe-O deformation in octahedral and tetrahedral sites, while the band at 470 cm^{-1} can be assigned to Fe–O deformation in octahedral sites of Fe_3O_4 [45,46]. In addition, 1148, 975 and 885 cm^{-1} bands can be ascribed to residual ethanol which was used for washing purpose at the end of synthesis protocol [47,48].

3.5. Electronic band gap analysis via DR-UV-VIS spectroscopy

DR-UV-VIS spectra of the synthesized pure and Fe-doped *mpg*-C_3N_4 photocatalysts are shown in Fig. 5. All of the *mpg*-C_3N_4 photocatalysts show comparable absorption line shape due to the excitation of electrons and charge transfer from valence band comprised mainly of N*2p* states to the conduction band which is mostly formed by C*2p* states [49]. Increasing the calcination temperature from 450 °C to 550 °C during the *mpg*-C_3N_4 synthesis protocol leads to a gradual red shift in the absorption edge which can be associated with the enhancement of electron delocalization and conjugation in the aromatic sheets as a result of increasing crystallographic order. Subsequently, the band gap energy decreases from *ca.* 2.74 eV to 2.72, and 2.70 eV, as the calcination temperature is gradually increased from 450 °C to 500 °C, and 550 ^{0}C, respectively. Incorporation of Fe_3O_4 into *mpg*-CN500 structure has two noticeable effects in the DR-UV-VIS spectra. Firstly, it enhances the absorption intensity. Secondly, it leads to a further red shift in the absorption edge (*i.e.* 2.65 eV). This additional red shift in the absorption edge of Fe_3O_4/*mpg*-CN500 photocatalyst may facilitate the electron–hole pair generation under VIS-light irradiation, which in turn, can result in improved photocatalytic efficiency [50]. Fe_3O_4 NPs are dispersed on/within the layers and pores of *mpg*-C_3N_4. We believe that –CN, -NH_2, -NO_x, -$C_xH_yO_z$ terminations/functional groups/structural defects of *mpg*-C_3N_4 provide binding sites for Fe_3O_4 NPs. In addition, oleylamine capping agent of Fe_3O_4 NP might also provide additional binding capabilities with the *mpg*-C_3N_4 layers. In addition to these, other point defects, extended defects (*e.g.* edges, kinks), corners and/or termination sites could also be other possible sites for Fe_3O_4 NP accommodation.

3.6. Specific surface area analysis via BET

Specific surface area (SSA) of *mpg*-C_3N_4 materials were determined by BET nitrogen adsorption isotherms. The specific surface area of *mpg*-CN450, *mpg*-CN500, *mpg*-CN550 and Fe_3O_4/*mpg*-CN500 photocatalysts were found to be 67, 140, 165 and 130 m^2/g, respectively. The increase in SSA with increasing calcination temperatures is due to the enhanced endothermic decomposition of guanidine hydrochloride at higher temperatures resulting in the formation of a porous *mpg*-C_3N_4 network with a higher SSA. On the other hand, anchoring of Fe_3O_4 NPs on mpg-C_3N_4 leads to a minor decrease in SSA, which can be attributed to the partial blocking of the *mpg*-C_3N_4 pores by Fe_3O_4 NPs with an average diameter of *ca.* 10 nm (Fig. 1a andb).

3.7. Photocatalytic NO_x(g) oxidation and storage (PHONOS) in solid state

In order to demonstrate catalytic activity of the currently synthesized *mpg*-C_3N_4 photocatalysts, we performed photocatalytic NO_x(g) oxidation and storage (PHONOS) tests using a custom-made photocatalytic flow reactor. It is well known that the ultimate predominant form of the stored NO_x species on the photocatalyst surface is nitrate and HNO_3 species [51]. The term "NO_x Storage" is a very commonly used term in catalysis, particularly for DeNOx catalytic converters used in tail-pipe emission control systems of diesel engines. Such non-photocatalytic DeNOx catalysts (*e.g.* NOx Oxidation and Storage, NSR catalysts, also called Lean NOx Traps, LNT) are also commercially utilized, where NO(g) and NO_2(g) are stored on solid oxide catalysts in the form of nitrites and nitrates [6–8]. Along these lines, VIS-light induced removal of NO(g) was monitored under *in-situ* conditions for different *mpg*-C_3N_4 photocatalysts. Fig. 6 shows a typical set of time-dependent NO(g), NO_2(g) and total NO_x(g) concentration profiles as a function of irradiation time during the NO photo-oxidation over Fe_3O_4/*mpg*-CN500 photocatalyst. In the first stage of the photocatalytic activity tests, a synthetic polluted air gas mixture containing *ca.* 1 ppm NO(g) was fed to the photocatalyst surface under dark conditions. During this initial phase (*i.e.* first 15 min), a minor transitory fall in the total NO_x(g) and NO(g) concentrations was observed due to adsorption of NO_x species on the reactor lines, expansion of the gas in the reactor as well as non-photocatalytic adsorption of NO_x on the photocatalyst surface. In addition, a tiny amount of NO_2(g) was produced due to thermal catalytic disproportionation processes occurring on the catalyst surface. Following the saturation of the reactor system and photocatalyst surface, NO_x(g) and NO(g) levels quickly returned to the original inlet concentration and reached a steady state in dark conditions.

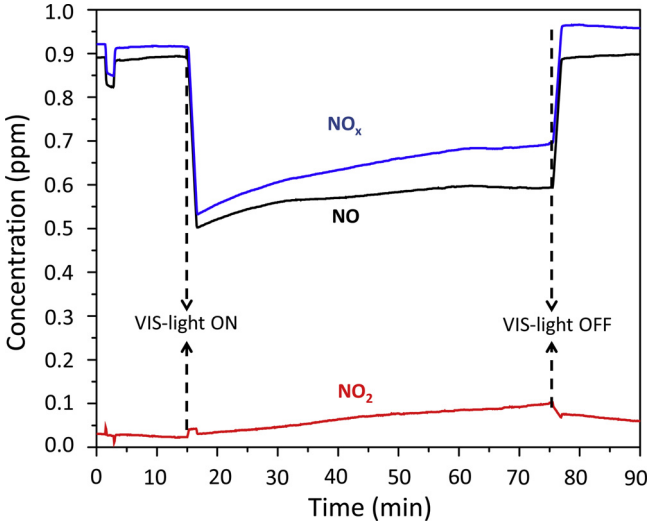

Fig. 6. Concentration *versus* time profiles obtained during a typical Photocatalytic NO_x(g) Oxidation and Storage (PHONOS) activity test performed on Fe_3O_4/*mpg*-CN500 photocatalyst in a custom-made photocatalytic flow reactor. Red, black and blue traces correspond to NO_2(g), NO(g) and total NO_x (*i.e.* NO(g) + NO_2) concentrations measured (with a 1 Hz acquisition rate) as a function of time during the photocatalytic activity test. Feed composition: N_2 (g) 0.750 SLM, O_2(g) 0.250 SLM, and NO(g) 0.010 SLM (100 ppm NO (g) diluted in balance N_2 (g), RH 50% at 23 °C.

Next, VIS-light irradiation was turned on after the first *ca.* 15 min (Fig. 6) and a drastic fall in the NO(g) and total NO_x(g) concentrations was detected along with a small increase in the NO_2(g) level. While the latter observation suggests the photocatalytic oxidation of NO(g) into NO_2(g), fall in the NO(g) and total NO_x(g) concentrations indicates the solid state storage of NO(g) and NO_2(g) in the form of chemisorbed NO_2, nitrites and/or nitrates on the *mpg*-C_3N_4 surface [8,52]. In principle, N_2(g) and/or N_2O(g) can also be produced as a result of direct photocatalytic decomposition and photo-reduction of NO(g) [53]. However, this is known to be a relatively inefficient reaction pathway, particularly in the presence of H_2O(g) and thus can readily be ruled out in the current study as a minor photocatalytic route [54]. It is apparent in Fig. 6 that photocatalytic NO_x abatement action continues in an uninterrupted manner after this initial stage during the entire duration of the activity test. Thus, total NO_x abatement effect can be calculated by integrating the relevant traces for the total PHONOS test duration (see SI section for the details of such calculations).

Photocatalytic NO_x(g) oxidation and storage (PHONOS) activity tests were performed for all of the *mpg*-C_3N_4-based photocatalysts and compared with that of a commercial benchmark titania P25 photocatalyst under identical experimental conditions (Figs. 7–9). Fig. 7 presents the photocatalytic activity data in terms of NO_x storage photonic efficiency % and NO_2(g) production photonic efficiency % values (which are normalized by the corresponding VIS-photon flux values), while Fig. 8 illustrates the absolute NO(g) conversion % and NO_2 storage selectivity % values. Meanwhile, overall photocatalytic NO_x abatement performances of all of the investigated photocatalysts are presented in Fig. 9 in terms of their corresponding DeNO$_x$ index values. Occupational Safety and Health Administration (OSHA), Association Advancing Occupational and Environmental Health (ACGIH) and The National Institute for Occupational Safety and Health (NIOSH) regulations suggest an environmental hazard limit value of 25 ppm for NO(g). On the other hand, corresponding limit value for NO_2(g) varies from 1 to 3 ppm, making NO_2(g) 8–25 times more toxic than NO(g) [55]. Based on these references, we have conservatively assigned a relative toxicity value of 1 to NO(g) and 3 to NO_2(g) [15] (see SI for more info). It is worth mentioning that per cent photonic efficiencies presented in Fig. 7 may seem relatively low (*i.e.* < 0.03%) and this is due to the VIS photon flux normalization. On the other hand, it should be noted that the corresponding percent conversion and selectivity values obtained

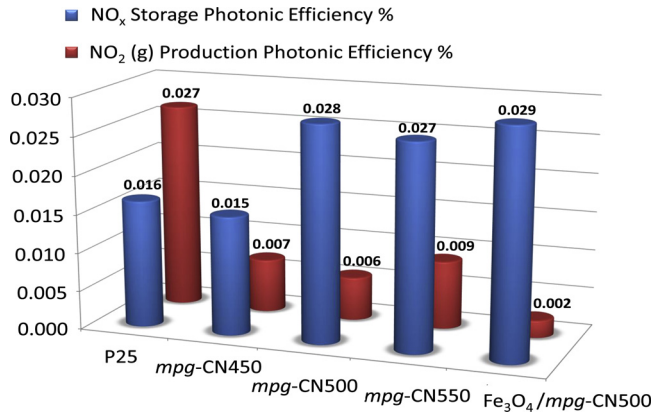

Fig. 7. NO_x storage photonic efficiency % (blue bars) and NO_2 (g) production photonic efficiency % (red bars) values for *mpg*-CN450, *mpg*-CN500, *mpg*-CN550 and Fe_3O_4/*mpg*-CN500 photocatalysts obtained *via* Vis-light irradiation.

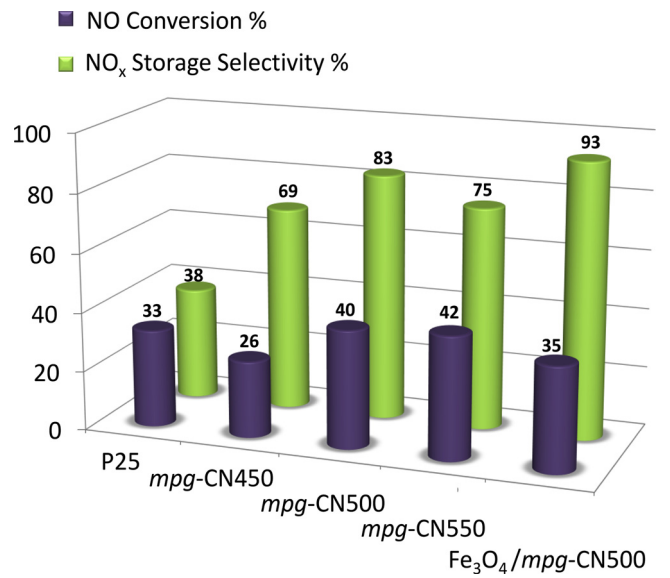

Fig. 8. NO(g) conversion % (purple bars) and NO_2 storage selectivity % (green bars) values for *mpg*-CN450, *mpg*-CN500, *mpg*-CN550 and Fe_3O_4/*mpg*-CN500 photocatalysts obtained *via* Vis-light irradiation.

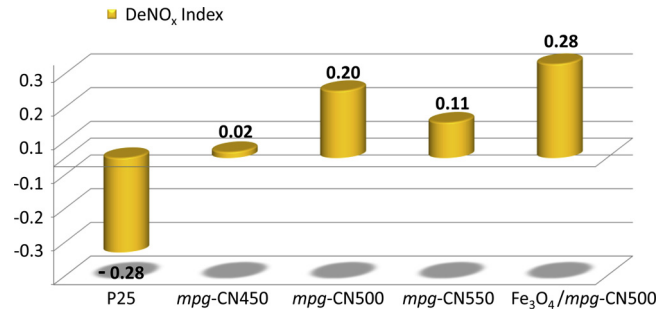

Fig. 9. $DeNO_x$ index values for *mpg*-CN450, *mpg*-CN500, *mpg*-CN550 and Fe_3O_4/*mpg*-CN500 photocatalysts obtained *via* Vis-light irradiation.

without photon flux normalization (Fig. 8) are quite high (*i.e.* 33–93 %).

It is important to note that absolute photocatalytic conversion and selectivity values are highly sensitive to reaction conditions and reactor design. This has been an important and well-known challenge for the comparison of literature data obtained by different groups using different experimental parameters. Hence, use of a benchmark catalyst and reporting "relative values with respect to a benchmark" is the most effective method for data comparison. On the other hand, choice of the benchmark catalyst should be made in such a way that it allows comparison of the maximum number of independent research studies published in the literature. Along these lines, P25 form of titania was chosen in the current work as the benchmark catalyst since this is probably the most commonly used photocatalyst in the literature.

It is clear from Figs. 7 and 8 that titania P25 commercial benchmark photocatalyst has a reasonably high NO_x storage efficiency. On the other hand, this titania benchmark catalyst simultaneously produces a very large quantity of unwanted NO_2(g). Despite the fact that the adsorption capacity of TiO_2 for NO_2(g) is much higher than that for NO(g) [56], photocatalytic NO_2(g) production rate and the total amount of NO_2 generated readily overwhelms the NO_x adsorption capacity of titania leading to unwanted NO_2(g) slip/release into the atmosphere. As NO_2(g) is a much more toxic pollutant than NO(g), P25 does not qualify as an efficient photocatalyst for NO_x abatement under visible light irradiation, evident by the extremely negative $DeNO_x$ index of P25 (-0.28) given in Fig. 9.

When the corresponding photocatalytic performances of *mpg*-C_3N_4-based photocatalysts are investigated (Figs. 7–9), striking improvements can be readily noticed as opposed to that of titania P25 commercial benchmark photocatalyst such as increased percent NO_x storage photonic efficiency and decreased NO_2(g) production photonic efficiency (Fig. 7), increased NO conversion %, increased NO_x storage selectivity % (Fig. 8), and increased $DeNO_x$ index (Fig. 9) values.

Comparison of the relative photocatalytic performance of pure *mpg*-C_3N_4 photocatalysts (*i.e.* *mpg*-CN450, *mpg*-CN500, *mpg*-CN550) in Figs. 7–9 clearly reveals a volcano-plot like behavior suggesting that in the absence of Fe incorporation, *mpg*-CN500 photocatalyst demonstrates the optimum performance by maximizing photocatalytic NO_x oxidation and storage, while minimizing the NO_2(g) release to the atmosphere. As opposed to P25 titania commercial benchmark photocatalyst, NO conversion % was improved from 33% to 40% and NO_x storage selectivity % was enhanced from 38% to 83% on *mpg*-CN500 (Fig. 8). On the other hand, negative $DeNO_x$ index of P25 titania commercial benchmark photocatalyst (-0.28) was radically surpassed by the *mpg*-CN500 photocatalyst (+0.20, Fig. 9). In other words, while P25 titania commercial benchmark photocatalyst does not reveal a net NO_x abatement effect under VIS irradiation, *mpg*-CN500 photocatalyst reveals a strong photocatalytic detoxification action under VIS-light.

Superior photocatalytic performance of *mpg*-CN500 over titania P25 can originate from two major functional improvements associated with *mpg*-CN500. Firstly, *mpg*-CN500 can perform NO(g) photo-oxidation with a greater effectiveness, possibly due to its favorably lower electronic band gap (2.72 *vs.* 3.1 eV), greater electron-hole generation capability, better charge migration, longer life-time of charge carriers and well-dispersed photocatalytic active sites over the mesoporous *mpg*-C_3N_4 2D-layers allowing efficient harvesting of VIS-light. Secondly, surface functional groups of *mpg*-CN500, structural defects and the unique termination sites as well as the relatively higher specific surface area of *mpg*-C_3N_4 as compared to that of P25 results in enhanced NO_x-capture and storage in the solid state on *mpg*-CN500. It is worth mentioning that enhanced photocatalytic performance of *mpg*-CN500 over P25 titania or other *mpg*-C_3N_4 photocatalysts cannot be solely attributed to the greater SSA of the former photocatalyst but rather involves various structural/electronic/surface chemical properties of *mpg*-CN500 discussed above and further examined in the later part of this report. Different photocatalysts can exhibit same photoactivity despite having comparatively different surface areas, because activity is rate-limited by photoreaction rather than adsorption [57]. For instance, although SSA of *mpg*-CN550 (165 m^2/g) is greater than that of *mpg*-CN500 (140 m^2/g), *mpg*-CN550 demonstrates a lower photocatalytic activity as compared to *mpg*-CN500.

In their detailed mechanistic study, Bloh et al. [51] suggested that there may be two opposing molecular pathways governing the overall selectivity in PHONOS process. It is well known that the ultimate predominant form of the stored NO_x species in the solid state is nitrate and HNO_3 species adsorbed on the photocatalyst surface. Thus, in order to maximize the activity and selectivity of the photocatalyst, one needs to maximize nitrate coverage on the surface without facilitating NO_2(g) release. However, it was reported that [51], there is a trade-off between nitrate coverage and NO_2(g) release, where increasing nitrate surface coverage may trigger unwanted NO_2(g) production with the assistance of conduction band electrons generated by the photon absorption. In other words, it was proposed that the origin of NO_2(g) generation in PHONOS process is the reduction of surface nitrates. An effective strategy to circumvent this problem was suggested to consider electron scavengers which can suppress nitrate reduction by facilitating O_2 reduction to form surface superoxide and hydroperoxyl radicals (with the assistance of H^+(ads) species). Therefore, the use of co-catalysts which can scavenge electrons from the nitrate reduction pathways, while facilitating molecular oxygen reduction could significantly enhance selectivity of the PHONOS systems without sacrificing their photocatalytic activity (*i.e.* conversion). Along these lines, FeO_x

semiconductor nanoparticles containing Fe^{2+} and Fe^{3+} redox sites (such as the currently used Fe_3O_4 nanoparticles containing minority Fe_2O_3 surface domains) could be a promising alternative to boost the selectivity of *mpg*-C_3N_4 photocatalysts without sacrificing their photocatalytic activity.

As stated above, NO_2 is a poisonous intermediate and must be avoided. Adsorbed oxygen on the catalyst surface can compete with nitrates for electrons and suppress the formation of NO_2. However, the reduction of nitrates to NO_2 is thermodynamically favored as compared to molecular oxygen reduction. To address this problem, an FeO_x co-catalyst can be introduced which can promote oxygen reduction. Until now, high selectivity towards solid state NO_x storage and prevention of gaseous NO_2 formation have been achieved either *via* utilization of precious metals [58–60] or this selectivity increase was achieved at the expense of a sacrifice in absolute activity [15,61]. In this regard, non-precious transition metals present an effective and convenient alternative to counter these drawbacks and increase the oxygen reduction capabilities of photocatalysts [62,63]. Here, we propose the introduction of Fe_3O_4 onto *mpg*-C_3N_4 photocatalyst to suppress the release of NO_2 during photo-oxidation of NO. The acceleration in the oxygen reduction with the assistance of Fe_3O_4 can allow a larger number of holes to oxidize the desired compounds (*i.e.* NO and NO_2) [64]. The resultant modification can improve the optical absorption range, as well as the charge carrier transfer rate in Fe_3O_4/*mpg*-C_3N_4, ultimately resulting in improved activity and selectivity [65].

Figs. 7–9 clearly demonstrate that this is an efficient strategy. It is evident that incorporation of FeO_x species into the optimized *mpg*-C_3N_4 photocatalyst (*i.e.* *mpg*-CN500) to form Fe_3O_4/*mpg*-CN500 photocatalyst leads to a further enhancement of overall photocatalytic performance by leading to a *ca.* 40% boost in $DeNO_x$ index (Fig. 9) from +0.20 (*mpg*-CN500) to +0.28 (Fe_3O_4/*mpg*-CN500) under VIS-light illumination. This is accomplished by a substantial increase in NO_x storage selectivity to 93% with only a minor decrease in NO conversion % to 35% (Fig. 8).

Currently observed synergistic effect associated with the FeO_x doping of *mpg*-C_3N_4 photocatalysts can also be attributed to the lowering of the electronic band gap energy (2.65 eV) and reduced recombination rate of photo-generated electron-hole pairs. The latter argument can be supported by considering the fact that the reduction potential of Fe^{2+}/Fe^{3+} is below the conduction band of g-C_3N_4 [30]. We believe that Fe^{2+}/Fe^{3+} species can act as electron scavengers in Fe_3O_4/*mpg*-CN500 photocatalysts where photo-generated electrons are trapped by the Fe_3O_4 doping sites, resulting in a decrease in the recombination rates of photo-generated electron–hole pairs.

As can be seen in Fig. 8, NO conversion % is slightly lower for Fe_3O_4/*mpg*-CN500 (35%) as compared to that of *mpg*-CN500 (40%) which is probably due to the loss of specific surface area after doping (130 *vs.* 140 m^2/g, respectively). Fe_3O_4/*mpg*-CN500 photocatalyst performed remarkably better, when compared with similar *g*-C_3N_4 based photocatalyst systems in terms of conversion%, selectivity% and DeNOx Index under VIS light illumination [66–68]. Further studies are underway in our group towards exploring the optimum Fe_3O_4 loading.

3.8. Photoluminescence (PL)

In order to elucidate the origins of the differences in photocatalytic NOx oxidation performance of the currently investigated samples, PL experiments were carried out. PL experiments revealed information regarding the migration, transfer, and recombination processes of photoinduced electron − hole pairs in the *mpg*-C_3N_4 systems. Fig. 10 shows the PL spectra of *mpg*-CN450, *mpg*-CN500, *mpg*-CN550 and Fe_3O_4/*mpg*-CN500 obtained with an excitation wavelength of 390 nm at room temperature. A strong emission peak was observed for *mpg*-CN450 indicating higher recombination rate of excited electrons and holes, ultimately leading to a lower photocatalytic efficiency [69]. As the *mpg*-C_3N_4 synthesis temperature increases, PL emission peak intensity

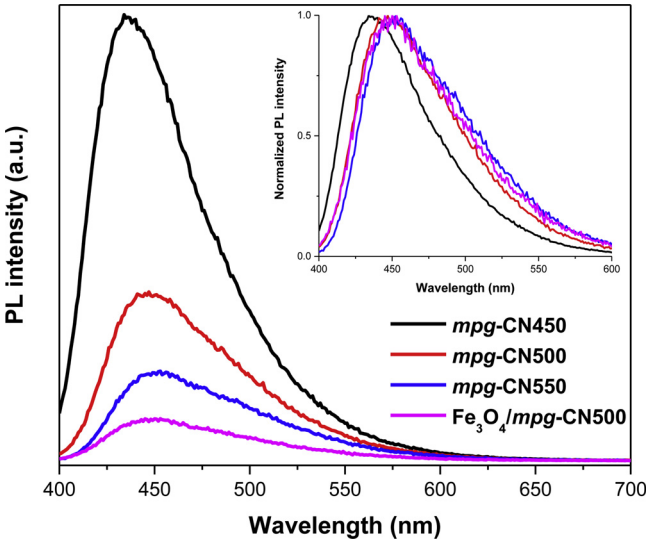

Fig. 10. PL spectra of *mpg*-CN450, *mpg*-CN500, *mpg*-CN550 and Fe_3O_4/*mpg*-CN500 photocatalysts (λ_{ex} = 390 nm). Intensity-normalized spectra are shown in the inset.

decreases significantly for *mpg*-CN500 and *mpg*-CN550, resulting in better photocatalytic performance of these two materials as compared to *mpg*-CN450. For Fe_3O_4/*mpg*-CN500, PL intensity further decreases in a notable manner, indicating a much lower recombination rate of photoinduced electron − hole pairs. This probably happens because photoinduced electrons can easily migrate from the conduction band (CB) of *mpg*-CN500 to the CB of Fe_3O_4 (*i.e.* away from the holes), thanks to the energy matching band structure of the Fe_3O_4/*mpg*-CN500 composite system [49]. Moreover, Fe_3O_4 has a relatively fast electron transport rate due to its high conductivity which suppresses the direct recombination of photo-induced electron − hole pairs in the Fe_3O_4/*mpg*-CN500 system [22]. The electrons in the CB of Fe_3O_4 are good reductants that can efficiently reduce the O_2 species adsorbed on the photocatalyst surface to various reactive species (*e.g.* superoxide and hydroperoxyl radicals), consequently suppressing the reduction of nitrates to NO_2 and leading to enhanced photocatalytic oxidation of NO_x.

It is interesting to note here that, although PL spectra show significantly low emission intensity for *mpg*-CN550, it has comparatively low photocatalytic efficiency as compared to *mpg*-CN500 (Figs. 7–9). Upon closer inspection of IR spectra in Fig. 4, it becomes evident that *mpg*-CN550 structure has cyanide/cyano defects (2181 cm^{-1}) which could reduce the electron mobility on the π conjugation plane of g-C_3N_4. For *mpg*-CN550, we believe that non-radiative (thermal) relaxation channels could be responsible for the decrease in the free charge carrier concentration, subsequently resulting in reduced photocatalytic ability [70,71]. To a lesser extent, this adverse effect can also be observed for the NO conversion on Fe_3O_4/*mpg*-CN500 photocatalyst (Fig. 4 and 8).

The inset in Fig. 10 shows that centers of PL spectra shift with the increase of processing temperatures (435 nm for *mpg*-CN450, 447 nm for *mpg*-CN500 and 453 nm for *mpg*-CN550), indicating the gradual development of defects in the material. Additionally, the full width at half maximum (FWHM) also becomes broader with the increasing temperature due to the changes in degree of thermal condensation and microstructural order in the *mpg*-C_3N_4 photocatalysts [72,73]. These results suggest that extent of polymerization of the precursor and the concentration of cyano/cyanide trap sites play an important role in the overall photocatalytic activity of the *mpg*-C_3N_4 photocatalysts. In addition, different precursors and utilization of various purification methods might also influence the type and concentration of defects in the *mpg*-C_3N_4 system, which may allow further fine tuning of photocatalytic performance [70].

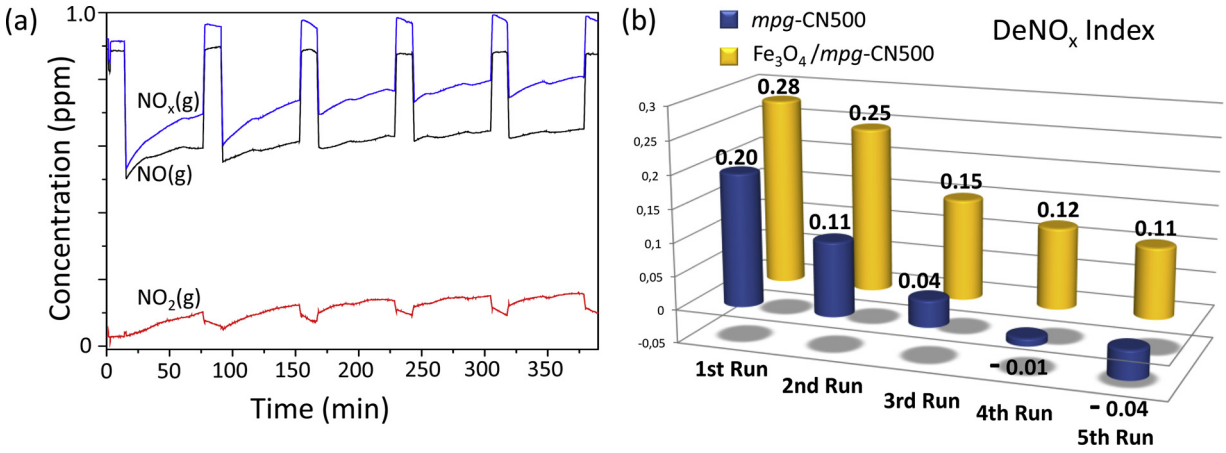

Fig. 11. (a) Concentration *versus* time curves for catalytic reusability test of Fe_3O_4/*mpg*-CN500 photocatalysts where the photocatalyst was exposed to 5 subsequent identical PHONOS runs under VIS-light irradiation, (b) corresponding $DeNO_x$ index values for *mpg*-CN500 and Fe_3O_4/*mpg*-CN500 photocatalysts calculated for each run of the reusability tests.

3.9. Photochemical stability of mpg-C_3N_4 based photocatalysts and reusability

Photochemical-stability and reusability of photocatalysts are crucial properties for end user applications. Thus, in order to demonstrate the reusability of the currently investigated materials, we performed a series of experiments. In these experiments, five successive VIS-light induced photo-oxidation tests were performed for two of the best performing photocatalyst (*i.e.* *mpg*-CN500 and Fe_3O_4/*mpg*-CN500) under identical reaction conditions. It must be stated here that no regeneration treatment was performed for these photocatalysts during these reaction cycles. As shown in Fig. 11, the $DeNO_x$ index value gradually decreased for *mpg*-CN500 after each cycle and became negative after the fourth cycle. This monotonic attenuation in NOx abatement capability could be probably due to the continuous accumulation of nitrites on the photocatalyst surface diminishing the NO_x storage capacity and facilitating NO_2(g) generation by nitrate reduction. While a monotonic decrease in $DeNO_x$ index was also visible for the Fe_3O_4/*mpg*-CN500 photocatalyst, attenuation in the $DeNO_x$ index values was significantly smaller in magnitude resulting in positive $DeNO_x$ index values for all cycles. Note that identical re-usability experiments performed with P25 titania benchmark catalysts (data not shown) also revealed a monotonically decreasing $DeNO_x$ index values where the values ranged between -0.30 and -0.40.

These results clearly indicate that the Fe_3O_4/*mpg*-CN500 photocatalyst has excellent long-term stability and enhanced activity. The slight decrease in photocatalytic activity of Fe_3O_4/*mpg*-CN500 photocatalyst with time is primarily due to the accumulation of surface nitrate species which can be easily regenerated by washing the photocatalyst with water [74]. In other words, Fe_3O_4/*mpg*-CN500 photocatalyst architecture can be considered as a highly active, selective, stable and an affordable material that can be synthesized readily in large scales and applied in outdoor NO_x abatement applications.

4. Conclusion

In the current work, highly efficient Fe_3O_4 NPs anchored *mpg*-C_3N_4 photocatalysts were synthesized by a facile and cost-effective synthetic protocol. Fe_3O_4/*mpg*-CN500 photocatalyst revealed significantly superior photocatalytic NO_x abatement performance under visible light as compared to the commercial P25 titania benchmark photocatalyst. Fe species in the Fe_3O_4/*mpg*-CN500 photocatalyst structure existed as FeO_x nanoparticles with an average diameter of *ca.* 10 nm on *mpg*-C_3N_4 surface. Incorporation of the Fe species to the photocatalyst formulation enhanced the total light absorption in the visible region, decreased the electronic band gap of *mpg*-C_3N_4 and also generated structural defects resulting in crystallographic disorder. Introduction of FeO_x species significantly increased the oxygen reduction capacity of *mpg*-CN500 resulting in lower NO_2 production which ultimately resulted in enhanced selectivity in photocatalytic NO_x abatement. Fe_3O_4/*mpg*-CN500 photocatalyst showed high activity, selectivity and stability even after five successive experimental runs without any regeneration step. Enhanced photocatalytic efficiency could be mainly attributed to the unique mesoporous structure, high surface area, enhanced charge separation efficiency and prolonged life time of charge carriers. Further studies are ongoing in our research group for elucidating the detailed photocatalytic mechanism, influence of Fe loading, effect of temperature and influence of regeneration methodology. We believe that Fe_3O_4/*mpg*-CN500 presents itself as an example of a new family of affordable, active, scalable and environmentally friendly photocatalytic materials which has a significant potential in environmental remediation and solar energy conversion applications.

Acknowledgements

EO, MI, MB, YK acknowledge the financial support from the Scientific and Technological Research Council of Turkey (TUBITAK) (Project Code: 116M435). EO acknowledges the scientific collaboration with TARLA project founded by the Ministry of Development of Turkey (project code: DPT2006K – 120,470). ÖM thanks to the Turkish Academy of Sciences for the financial support.

Appendix A. Supplementary data

Supplementary material related to this article can be found, in the online version, at doi:https://doi.org/10.1016/j.apcatb.2019.02.067.

References

[1] K. Skalska, J.S. Miller, S. Ledakowicz, Trends in NOx abatement: a review, Sci. Total Environ. 408 (2010) 3976–3989.
[2] J. Ma, H. Wu, Y. Liu, H. He, Photocatalytic removal of NOx over visible light responsive oxygen-deficient TiO2, J. Phys. Chem. C 118 (2014) 7434–7441.
[3] U. Gehring, O. Gruzieva, R.M. Agius, R. Beelen, A. Custovic, J. Cyrys, M. Eeftens, C. Flexeder, E. Fuertes, J. Heinrich, B. Hoffmann, J.C. de Jongste, M. Kerkhof, C. Klumper, M. Korek, A. Molter, E.S. Schultz, A. Simpson, D. Sugiri, M. Svartengren, A. von Berg, A.H. Wijga, G. Pershagen, B. Brunekreef, Air pollution exposure and lung function in children: the ESCAPE project, Environ. Health Perspect. 121 (2013) 1357–1364.
[4] A. Folli, S.B. Campbell, J.A. Anderson, D.E. Macphee, Role of TiO2 surface hydration on NO oxidation photo-activity, J. Photochem. Photobiol. A: Chem. 220 (2011) 85–93.
[5] S. Roy, M.S. Hegde, G. Madras, Catalysis for NOx abatement, Appl. Energy 86

(2009) 2283–2297.
[6] Z. Say, O. Mihai, M. Kurt, L. Olsson, E. Ozensoy, Trade-off between NOx storage capacity and sulfur tolerance on Al2O3/ZrO2/TiO2–based DeNOx catalysts, Catal. Today 320 (2019) 152–164.
[7] Z. Say, M. Tohumeken, E. Ozensoy, NOx storage and reduction pathways on zirconia and titania functionalized binary and ternary oxides as NOx storage and reduction (NSR) systems, Catal. Today 231 (2014) 135–144.
[8] S.M. Andonova, G.S. Şentürk, E. Ozensoy, Fine-tuning the dispersion and the mobility of BaO domains on NOx storage materials via TiO2 anchoring sites, J. Phys. Chem. C 114 (2010) 17003–17016.
[9] J. Angelo, L. Andrade, A. Mendes, Highly active photocatalytic paint for NOx abatement under real-outdoor conditions, Appl. Catal. a-Gen. 484 (2014) 17–25.
[10] R. Sugrañez, J.I. Álvarez, M. Cruz-Yusta, I. Mármol, J. Morales, J. Vila, L. Sánchez, Enhanced photocatalytic degradation of NOx gases by regulating the microstructure of mortar cement modified with titanium dioxide, Build. Environ. 69 (2013) 55–63.
[11] C. Guo, X. Wu, M. Yan, Q. Dong, S. Yin, T. Sato, S. Liu, The visible-light driven photocatalytic destruction of NOx using mesoporous TiO2 spheres synthesized via a "water-controlled release process, Nanoscale 5 (2013) 8184–8191.
[12] M.M. Ballari, H.J.H. Brouwers, Full scale demonstration of air-purifying pavement, J. Hazard. Mater. 254-255 (2013) 406–414.
[13] H. Chen, C.E. Nanayakkara, V.H. Grassian, Titanium dioxide photocatalysis in atmospheric chemistry, Chem. Rev. 112 (2012) 5919–5948.
[14] M. Pelaez, N.T. Nolan, S.C. Pillai, M.K. Seery, P. Falaras, A.G. Kontos, P.S.M. Dunlop, J.W.J. Hamilton, J.A. Byrne, K. O'Shea, M.H. Entezari, D.D. Dionysiou, A review on the visible light active titanium dioxide photocatalysts for environmental applications, Appl. Catal. B 125 (2012) 331–349.
[15] J.Z. Bloh, A. Folli, D.E. Macphee, Photocatalytic NOx abatement: why the selectivity matters, RSC Adv. 4 (2014) 45726–45734.
[16] Z. Zhao, Y. Sun, F. Dong, Graphitic carbon nitride based nanocomposites: a review, Nanoscale 7 (2015) 15–37.
[17] D.A. Erdogan, M. Sevim, E. Kısa, D.B. Emiroglu, M. Karatok, E.I. Vovk, M. Bjerring, Ü. Akbey, Ö. Metin, E. Ozensoy, Photocatalytic activity of mesoporous graphitic carbon nitride (mpg-C3N4) towards organic chromophores under UV and VIS light illumination, Top. Catal. 59 (2016) 1305–1318.
[18] W.-J. Ong, L.-L. Tan, Y.H. Ng, S.-T. Yong, S.-P. Chai, Graphitic Carbon Nitride (g-C3N4)-Based Photocatalysts for Artificial Photosynthesis and Environmental Remediation: Are We a Step Closer To Achieving Sustainability? Chem. Rev. 116 (2016) 7159–7329.
[19] I. Papailias, N. Todorova, T. Giannakopoulou, N. Ioannidis, N. Boukos, C.P. Athanasekou, D. Dimotikali, C. Trapalis, Chemical vs thermal exfoliation of g-C3N4 for NOx removal under visible light irradiation, Appl. Catal. B 239 (2018) 16–26.
[20] Z. Zhao, Y. Dai, J. Lin, G. Wang, Highly-ordered mesoporous carbon nitride with ultrahigh surface area and pore volume as a superior dehydrogenation catalyst, Chem. Mater. 26 (2014) 3151–3161.
[21] V.I. Pârvulescu, P. Grange, B. Delmon, Catalytic removal of NO, Catal. Today 46 (1998) 233–316.
[22] S. Kumar, S.T.B. Kumar, A. Baruah, V. Shanker, Synthesis of magnetically separable and recyclable g-C3N4–Fe3O4 hybrid nanocomposites with enhanced photocatalytic performance under visible-light irradiation, J. Phys. Chem. C 117 (2013) 26135–26143.
[23] S. Xuan, W. Jiang, X. Gong, Y. Hu, Z. Chen, Magnetically separable Fe3O4/TiO2 hollow spheres: fabrication and photocatalytic activity, J. Phys. Chem. C 113 (2009) 553–558.
[24] X. Guangcheng, Y. Bing, C. Junyu, Y. Jinhua, Fe3O4/WO3 hierarchical core–shell structure: high-performance and recyclable visible-light photocatalysis, Chem. Eur. J. 17 (2011) 5145–5154.
[25] J. Xu, H.-T. Wu, X. Wang, B. Xue, Y.-X. Li, Y. Cao, A new and environmentally benign precursor for the synthesis of mesoporous g-C3N4 with tunable surface area, J. Chem. Soc. Faraday Trans. 15 (2013) 4510–4517.
[26] Z. Xu, C. Shen, Y. Hou, H. Gao, S. Sun, Oleylamine as both reducing agent and stabilizer in a facile synthesis of magnetite nanoparticles, Chem. Mater. 21 (2009) 1778–1780.
[27] ISO 22197-1, Fine Ceramics (advanced Ceramics, Advanced Technical Ceramics) – Test Method for Air-purification Performance of Semiconducting Photocatalytic Materials – Part 1: Removal of Nitric Oxide, (2007), pp. 1–11.
[28] S.J. Iyengar, M. Joy, T. Maity, J. Chakraborty, R.K. Kotnala, S. Ghosh, Colloidal properties of water dispersible magnetite nanoparticles by photon correlation spectroscopy, RSC Adv. 6 (2016) 14393–14402.
[29] S.C. Yan, Z.S. Li, Z.G. Zou, Photodegradation performance of g-C3N4 fabricated by directly heating melamine, Langmuir 25 (2009) 10397–10401.
[30] W. Xinchen, C. Xiufang, T. Arne, F. Xianzhi, A. Markus, Metal-containing carbon nitride compounds: a new functional organic–metal hybrid material, Adv. Mater. 21 (2009) 1609–1612.
[31] G. Algara-Siller, N. Severin, S.Y. Chong, T. Björkman, R.G. Palgrave, A. Laybourn, M. Antonietti, Y.Z. Khimyak, A.V. Krasheninnikov, J.P. Rabe, U. Kaiser, A.I. Cooper, A. Thomas, M.J. Bojdys, Triazine-Based Graphitic Carbon Nitride: a Two-Dimensional Semiconductor, Angew. Chem. Int. Ed. Engl. 53 (2014) 7450–7455.
[32] Y. Yuan, L. Zhang, J. Xing, M.I.B. Utama, X. Lu, K. Du, Y. Li, X. Hu, S. Wang, A. Genç, R. Dunin-Borkowski, J. Arbiol, Q. Xiong, High-yield synthesis and optical properties of g-C3N4, Nanoscale 7 (2015) 12343–12350.
[33] W. Lidong, D. Major, P. Paga, D. Zhang, M.G. Norton, D.N. McIlroy, High yield synthesis and lithography of silica-based nanospring mats, Nanotechnology 17 (2006) S298.
[34] D. Wilson, M.A. Langell, XPS analysis of oleylamine/oleic acid capped Fe3O4 nanoparticles as a function of temperature, Appl. Surf. Sci. 303 (2014) 6–13.
[35] E. Ozensoy, C.H.F. Peden, J. Szanyi, Low temperature H2O and NO2 coadsorption on θ-Al2O3/NiAl(100) ultrathin films, J. Phys. Chem. B 110 (2006) 8025–8034.
[36] X. Gao, Y. Li, X. Yang, Y. Shang, Y. Wang, B. Gao, Z. Wang, Highly permeable and antifouling reverse osmosis membranes with acidified graphitic carbon nitride nanosheets as nanofillers, J. Mater. Chem. A 5 (2017) 19875–19883.
[37] J. Ma, Q. Yang, Y. Wen, W. Liu, Fe-g-C3N4/graphitized mesoporous carbon composite as an effective Fenton-like catalyst in a wide pH range, Appl. Catal. B 201 (2017) 232–240.
[38] M. Miyachi, Y. Yamamoto, Y. Yamanoi, A. Minoda, S. Oshima, Y. Kobori, H. Nishihara, Synthesis of diazenido-ligated vanadium nanoparticles, Langmuir 29 (2013) 5099–5103.
[39] P. Hunmin, Y.D. Hyun, K.J. Young, K.W. Yong, C.Y. Han, L.Y. Hye, C.S. Hee, L.J. Sung, Selective formation of hägg Iron carbide with g-C3N4 as a sacrificial support for highly active Fischer–Tropsch synthesis, ChemCatChem 7 (2015) 3488–3494.
[40] T. Yamashita, P. Hayes, Analysis of XPS spectra of Fe2+ and Fe3+ ions in oxide materials, Appl. Surf. Sci. 254 (2008) 2441–2449.
[41] J. Zhou, H. Song, L. Ma, X. Chen, Magnetite/graphene nanosheet composites: interfacial interaction and its impact on the durable high-rate performance in lithium-ion batteries, RSC Adv. 1 (2011) 782–791.
[42] A. Thøgersen, J.H. Selj, E.S. Marstein, Oxidation effects on graded porous silicon anti-reflection coatings, J. Electrochem. Soc. 159 (2012) D276–D281.
[43] M. Konsolakis, Z. Ioakimidis, T. Kraia, G. Marnellos, Hydrogen production by ethanol steam reforming (ESR) over CeO2 supported transition metal (Fe, Co, Ni, Cu) catalysts: insight into the structure-activity relationship, Catalysts 6 (2016) 39.
[44] S. Liu, J. Yu, W. Wang, Effects of annealing on the microstructures and photoactivity of fluorinated N-doped TiO2, J. Chem. Soc. Faraday Trans. 12 (2010) 12308–12315.
[45] Ou. Rahman, S.C. Mohapatra, S. Ahmad, Fe3O4 inverse spinal super paramagnetic nanoparticles, Mater. Chem. Phys. 132 (2012) 196–202.
[46] T. Belin, N. Guigue-Millot, T. Caillot, D. Aymes, J.C. Niepce, Influence of grain size, oxygen stoichiometry, and synthesis conditions on the γ-Fe2O3 vacancies ordering and lattice parameters, J. Solid State Chem. 163 (2002) 459–465.
[47] J. Tan, L. Yang, Q. Kang, Q. Cai, In situ ATR-FTIR and UV-Visible spectroscopy study of photocatalytic oxidation of ethanol over TiO2 nanotubes, Anal. Lett. 44 (2011) 1114–1125.
[48] F. Dang, N. Enomoto, J. Hojo, K. Enpuku, Sonochemical synthesis of monodispersed magnetite nanoparticles by using an ethanol–water mixed solvent, Ultrason. Sonochem. 16 (2009) 649–654.
[49] X. Wang, K. Maeda, A. Thomas, K. Takanabe, G. Xin, J.M. Carlsson, K. Domen, M. Antonietti, A metal-free polymeric photocatalyst for hydrogen production from water under visible light, Nat. Mater. 8 (2008) 76.
[50] S. Tonda, S. Kumar, S. Kandula, V. Shanker, Fe-doped and -mediated graphitic carbon nitride nanosheets for enhanced photocatalytic performance under natural sunlight, J. Mater. Chem. A 2 (2014) 6772–6780.
[51] J. Patzsch, A. Folli, D.E. Macphee, J.Z. Bloh, On the underlying mechanisms of the low observed nitrate selectivity in photocatalytic NOx abatement and the importance of the oxygen reduction reaction, J. Chem. Soc. Faraday Trans. 19 (2017) 32678–32686.
[52] S.M. Andonova, G.S. Şentürk, E. Kayhan, E. Ozensoy, Nature of the Ti−Ba interactions on the BaO/TiO2/Al2O3 NOx storage system, J. Phys. Chem. C 113 (2009) 11014–11026.
[53] O. Carp, C.L. Huisman, A. Reller, Photoinduced reactivity of titanium dioxide, Prog. Solid State Chem. 32 (2004) 33–177.
[54] W. Lu, A.D. Olaitan, M.R. Brantley, B. Zekavat, D.A. Erdogan, E. Ozensoy, T. Solouki, Photocatalytic conversion of nitric oxide on titanium dioxide: cryo-trapping of reaction products for online monitoring by mass spectrometry, J. Phys. Chem. C 120 (2016) 8056–8067.
[55] R.J. Lewis, Sax's Dangerous Properties of Industrial Materials, 11 ed., John Wiley & Sons, Inc, Hoboken, New Jersey, 2004.
[56] L. Sivachandiran, F. Thevenet, P. Gravejat, A. Rousseau, Investigation of NO and NO2 adsorption mechanisms on TiO2 at room temperature, Appl. Catal. B 142-143 (2013) 196–204.
[57] R. Dillert, A. Engel, P. Gro, D.W. Lindner, Bahnemann, Light intensity dependence of the kinetics of the photocatalytic oxidation of nitrogen(ii) oxide at the surface of TiO2, J. Chem. Soc. Faraday Trans. 15 (2013) 20876–20886.
[58] K. Fujiwara, U. Müller, S.E. Pratsinis, Pd subnano-clusters on TiO2 for solar-light removal of NO, ACS Catal. 6 (2016) 1887–1893.
[59] Y. Hu, X. Song, S. Jiang, C. Wei, Enhanced photocatalytic activity of Pt-doped TiO2 for NOx oxidation both under UV and visible light irradiation: a synergistic effect of lattice Pt4+ and surface PtO, Chem. Eng. J. 274 (2015) 102–112.
[60] K. Fujiwara, S.E. Pratsinis, Single Pd atoms on TiO2 dominate photocatalytic NOx removal, Appl. Catal. B 226 (2018) 127–134.
[61] J.Z. Bloh, R. Dillert, D.W. Bahnemann, Ruthenium-modified zinc oxide, a highly active vis-photocatalyst: the nature and reactivity of photoactive centres, J. Chem. Soc. Faraday Trans. 16 (2014) 5833–5845.
[62] J. Balbuena, G. Carraro, M. Cruz, A. Gasparotto, C. Maccato, A. Pastor, C. Sada, D. Barreca, L. Sánchez, Advances in photocatalytic NOx abatement through the use of Fe2O3/TiO2 nanocomposites, RSC Adv. 6 (2016) 74878–74885.
[63] S. Neubert, D. Mitoraj, S.A. Shevlin, P. Pulisova, M. Heimann, Y. Du, G.K.L. Goh, M. Pacia, K. Kruczala, S. Turner, W. Macyk, Z.X. Guo, R.K. Hocking, R. Beranek, Highly efficient rutile TiO2 photocatalysts with single Cu(ii) and Fe(iii) surface catalytic sites, J. Mater. Chem. A 4 (2016) 3127–3138.
[64] M. Nishikawa, Y. Mitani, Y. Nosaka, Photocatalytic reaction mechanism of Fe(III)-Grafted TiO2 studied by means of ESR spectroscopy and chemiluminescence photometry, J. Phys. Chem. C 116 (2012) 14900–14907.

[65] X. Chen, J. Zhang, X. Fu, M. Antonietti, X. Wang, Fe-g-C3N4-Catalyzed oxidation of benzene to phenol using hydrogen peroxide and visible light, J. Am. Chem. Soc. 131 (2009) 11658–11659.
[66] I. Papailias, N. Todorova, T. Giannakopoulou, S. Karapati, N. Boukos, D. Dimotikali, C. Trapalis, Enhanced NO 2 abatement by alkaline-earth modified g-C 3 N 4 nanocomposites for efficient air purification, Appl. Surf. Sci. 430 (2017) 225–233.
[67] I. Papailias, N. Todorova, T. Giannakopoulou, J. Yu, D. Dimotikali, C. Trapalis, Photocatalytic activity of modified g-C3N4/TiO2 nanocomposites for NOx removal, Catal. Today 280 (2017) 37–44.
[68] F. Dong, M. Ou, Y. Jiang, S. Guo, Z. Wu, Efficient and durable visible light photocatalytic performance of porous carbon nitride nanosheets for air purification, Ind. Eng. Chem. Res. 53 (2014) 2318–2330.
[69] F.B. Li, X.Z. Li, The enhancement of photodegradation efficiency using Pt–TiO2 catalyst, Chemosphere 48 (2002) 1103–1111.
[70] P. Wu, J. Wang, J. Zhao, L. Guo, F.E. Osterloh, Structure defects in g-C3N4 limit visible light driven hydrogen evolution and photovoltage, J. Mater. Chem. A 2 (2014) 20338–20344.
[71] A. Luque, A. Martí, E. Antolín, C. Tablero, Intermediate bands versus levels in non-radiative recombination, Physica B Condens. Matter 382 (2006) 320–327.
[72] Y. Zhang, Q. Pan, G. Chai, M. Liang, G. Dong, Q. Zhang, J. Qiu, Synthesis and luminescence mechanism of multicolor-emitting g-C3N4 nanopowders by low temperature thermal condensation of melamine, Sci. Rep. 3 (2013) 1943.
[73] H. Zhang, A. Yu, Photophysics and photocatalysis of carbon nitride synthesized at different temperatures, J. Phys. Chem. C 118 (2014) 11628–11635.
[74] Z. Ai, W. Ho, S. Lee, L. Zhang, Efficient photocatalytic removal of NO in indoor air with hierarchical bismuth oxybromide nanoplate microspheres under visible light, Environ. Sci. Technol. 43 (2009) 4143–4150.